

## Supporting Information

### **Electrocatalytic Hydrogen Evolution Reaction by a Ni(N<sub>2</sub>O<sub>2</sub>) Complex Based on 2,2'-bipyridine**

Julia M. Dressel, Emma N. Cook, Shelby L. Hooe, Juan J. Moreno, Diane A. Dickie, and Charles W. Machan\*

\* - machan@virginia.edu; ORCID 0000-0002-5182-1138

JMD ORCID: 0000-0002-3601-9710; ENC ORCID: 0000-0002-0568-3600;

SLH ORCID: 0000-0002-6991-2273;

JJM ORCID: 0000-0003-1809-6170; DAD ORCID: 0000-0003-0939-3309

Department of Chemistry, University of Virginia,  
PO Box 400319, Charlottesville, VA 22904-4319

## Materials and Methods

### General

All chemicals and solvents (ACS or HPLC grade) were commercially available and used as received unless otherwise indicated. For all air-sensitive reactions and electrochemical experiments, HPLC-grade solvents were obtained as anhydrous and air-free from a PPT Glass Contour Solvent Purification System. Gas cylinders were obtained from Praxair (Ar as 5.0; O<sub>2</sub> as 4.0) and passed through activated molecular sieves prior to use. Gas mixing for variable concentration experiments was accomplished using a gas proportioning rotameter from Omega Engineering. UV-vis absorbance spectra were obtained on a Cary 60 from Agilent. An Anton-Parr Multiwave Pro SOLV, NXF-8 microwave reactor was used for microwave syntheses.

### Electrochemistry

All electroanalytical experiments were performed using a Metrohm Autolab PGSTAT302N potentiostat. Glassy carbon working ( $\varnothing = 3$  mm) and non-aqueous silver/silver chloride pseudoreference electrodes behind PTFE tips were obtained from CH Instruments. The pseudoreference electrodes were obtained by depositing chloride on bare silver wire in 10% HCl at oxidizing potentials and stored in a 0.1 M tetrabutylammonium hexafluorophosphate/*N,N*-DMF solution in the dark prior to use. The counter electrode was a glassy carbon rod ( $\varnothing = 3$  mm). All CV experiments were performed in a modified scintillation vial (20 mL volume) as a single-chamber cell with a cap modified with ports for all electrodes and a sparging needle. Tetrabutylammonium hexafluorophosphate (TBAPF<sub>6</sub>) was purified by recrystallization from ethanol and dried in a vacuum oven before being stored in a desiccator. All data were referenced to an internal ferrocene standard (ferrocenium/ferrocene reduction potential under stated conditions) unless otherwise specified. All voltammograms were corrected for internal resistance. Ferrocene was purified by sublimation prior to use.

### Bulk Electrolysis

Bulk electrolysis experiments were performed in a glass Pine H-cell with two compartments separated by a glass frit. A 60 mL stock solution of DMF with 0.1 M TBAPF<sub>6</sub> was prepared for each bulk electrolysis experiment. Approximately 25 mL of the stock solution was added to each half of the H-cell. One side of the H-cell contained the Ni(<sup>*p*</sup>-*tbu*dhbpy) **1** catalyst, any additional substrate, such as C<sub>6</sub>F<sub>5</sub>OH, and a glassy carbon rod working electrode. The other side of the H-cell contained approximately 0.075 M ferrocene as a sacrificial reductant along with a graphite rod counter electrode and a Ag/AgCl pseudoreference electrode. The electrolysis experiment was referenced by taking a CV of the side of the H-cell that contained the ferrocene solution. The H-cell was sealed with two septa that were connected by a piece of PTFE tubing which aided to maintain equal pressure between each half of the cell during the electrolysis. Before starting the electrolysis experiment, both sides of the H-cell were sparged with the desired gas for 20 minutes and the sealed cell was allowed to equilibrate for 30 minutes. The resistance between the two halves of the H-cell was measured using the *i*-interrupt procedure available in the NOVA software provided by Metrohm.

## Bulk Electrolysis Product Analysis

During bulk electrolysis experiments, either 150 or 250  $\mu\text{L}$  GC injections of the headspace were periodically taken for the detection and quantification of any gaseous products produced. After each bulk electrolysis experiment, the total volume of solution was measured. The total volume of the sealed H-cell was also measured to account for the total headspace volume for accurate quantification of gaseous products. A calibration curve for  $\text{H}_2$  (**Figure S20**) was used to quantify gaseous products produced during electrolysis experiments in the same manner as we previously reported.<sup>1</sup>

Analysis of gas phase products was done by sampling electrolysis headspace through syringe injections into an Agilent 7890B GC equipped with a specialty gas split column 5  $\text{\AA}$  mol sieve/Porabond Q column (15 m length; 0.320 mm diameter; 25.0  $\mu\text{m}$  film) and thermal conductivity detector with He as a carrier gas. A calibration curve for  $\text{H}_2$  was made in the H-cell with an experimental setup containing identical volumes of DMF in 0.1 M TBAPF<sub>6</sub> to those used during electrolysis. Known volumes of  $\text{H}_2$  were injected into the cell with stirring and 250  $\mu\text{L}$  injections of the headspace were taken for GC injections after equilibration. The limit of detection (LOD) and limit of quantitation (LOQ) for  $\text{H}_2$  in the GC were determined from seven consecutive injections at the lowest observable concentrations of the gaseous product. For  $\text{H}_2$ , the LOD was determined to be  $4.55 \times 10^{-6}$  moles and the LOQ was determined to be  $1.52 \times 10^{-5}$  moles.

## Calculation of Overpotential

The calculation of overpotential for  $\text{Ni}(\text{p}^{\text{-tbu}}\text{dhbpy})$  **1** was performed according to reported methods.<sup>2, 3</sup> The following equation was used for the determination of the reaction standard potential in V with respect to the  $\text{Fc}^+/\text{Fc}$  couple:

$$E_{\text{H}^+/\text{H}_2} = -0.662 \text{ V} - 0.059(\text{p}K_{\text{a}}) \quad \text{Eq (1)}$$

The  $\text{p}K_{\text{a}}$  for pentafluorophenol ( $\text{C}_6\text{F}_5\text{OH}$ ) in acetonitrile (MeCN) is reported as 20.1.<sup>4</sup> It was adjusted to approximate the  $\text{p}K_{\text{a}}$  of  $\text{C}_6\text{F}_5\text{OH}$  in DMF, which was 9.6, using a linear scaling relationship reported by Leito and coworkers.<sup>4</sup>

$$\text{p}K_{\text{a}}(\text{DMF}) = \text{p}K_{\text{a}}(\text{MeCN}) * 0.95 - 9.5 = 9.6 \quad \text{Eq (2)}$$

This is then substituted into Equation 1 to yield:

$$E_{\text{H}^+/\text{H}_2}(\text{F}_5\text{C}_6\text{OH}) = -1.23 \text{ V vs } \text{Fc}^+/\text{Fc} \quad \text{Eq (3)}$$

The  $E_{\text{cat}/2}$  determined experimentally for  $\text{Ni}(\text{p}^{\text{-tbu}}\text{dhbpy})$  **1** is  $-2.40 \text{ V vs } \text{Fc}^+/\text{Fc}$  for proton reduction (1.0 mM  $\text{Ni}(\text{p}^{\text{-tbu}}\text{dhbpy})$  **1** and 0.033 M  $\text{C}_6\text{F}_5\text{OH}$  under Ar saturation); the overpotential is:

$$\eta = |E_{\text{cat}/2} - E_{\text{H}^+/\text{H}_2}| = 1.17 \text{ V} \quad \text{Eq (4)}$$

## Computational Methods

DFT calculations were performed on the Rivanna High-Performance Computing Cluster at the University of Virginia using the Gaussian 16 program, Rev B.01.<sup>5</sup> The hybrid functional B3LYP<sup>6-9</sup> and the 6-31+G(d,p) basis set for all atoms<sup>10-12</sup> were used for all calculations. Unrestricted geometry optimizations were carried out without geometry constraints and dispersion effects were accounted for by using Grimme's D3 parameter set with Becke-Johnson (BJ) damping.<sup>13</sup> Bulk solvent effects (*N,N*-dimethylformamide = DMF) were included at the optimization stage with the SMD continuum model.<sup>14</sup> The stationary points and their nature as minima or saddle points (TS) were characterized by vibrational analysis, which also produced enthalpy (H), entropy (S) and Gibbs energy (G) data at 298.15 K. The minima connected by a given transition state were determined by Intrinsic Reaction Coordinate (IRC) calculations or by perturbing the transition states along the TS coordinate and optimizing to the nearest minimum. For the lowest energy spin states of each species, free energies were corrected to account for concentration effects and for errors associated with the harmonic oscillator approximation. Thus, according to Truhlar's quasi-harmonic approximation, all vibrational frequencies below 100 cm<sup>-1</sup> were set to this value.<sup>15</sup> All anharmonic and concentration corrections were calculated with the Goodvibes code.<sup>16</sup> Concentrations of DMF was set to 12.92 M, C<sub>6</sub>F<sub>5</sub>OH to 50 mM, and all other species, including metal complexes, to 1.00 mM. Energies were then refined by performing single point optimizations with the 6-311+G(2d,p) basis set. The stability of these wavefunctions was verified at the triple-zeta level of theory.

The redox potentials were calculated relative to the phenazine (PHNZ) redox couple PHNZ/PHNZ<sup>0/1-</sup> and referenced to the ferrocene (Fc) redox couple Fc<sup>+/Fc</sup> based on experimental values in a manner described previously.<sup>17, 18</sup>

### Synthesis of 2,2'-([2,2'-bipyridine]-6,6'-diyl)bis(4-(tert-butyl)phenol), $P^{t\text{-bu}}\text{dhbpy}(\text{H}_2)$

The preparation of (5-tert-butyl-2-hydroxy-phenyl)boronic acid was carried out in similar fashion to the previously reported (3,5-di-tert-butyl-2-hydroxyphenyl)boronic acid.<sup>19</sup> Subsequent microwave-assisted Suzuki-type cross coupling of 6,6'-dibromo-2,2'-bipyridine with (5-tert-butyl-2-hydroxy-phenyl)boronic acid was also analogous to our previous synthetic method.<sup>1</sup> To a single microwave tube were added 6,6'-dibromo-2,2'-bipyridine (1.20 g, 0.382 mmol), sodium carbonate (3.50 g, 4.19 mmol), Pd(PPh<sub>3</sub>)<sub>4</sub> (0.0767 g, 0.0664 mmol), and (5-tert-butyl-2-hydroxy-phenyl)boronic acid (1.85 g, 0.955 mmol), degassed toluene (50 mL), degassed DI water (10 mL), and degassed methanol (12 mL). The microwave was set to run for 120 minutes at 170 °C at the highest ramp rate. After the reaction mixture had cooled, the aqueous and organic layers were separated. The aqueous layer was extracted with dichloromethane (DCM) (2 x 50 mL) and the organic layer was washed with brine (3 x 50 mL). The organic layers were combined, dried over MgSO<sub>4</sub>, and condensed to dryness. The product was loaded onto neutral alumina and purified via flash chromatography with the following conditions: 30% DCM in hexanes for 5 min, 40% DCM for 15 min, gradual increase to 100% DCM for 5 min and hold for 10 min. Pure, unreacted 6,6'-dibromo-2,2'-bipyridine eluted first, followed by the  $P^{t\text{-bu}}\text{dhbpy}(\text{H}_2)$  ligand (1.3 g, 75% isolated yield). <sup>1</sup>H NMR (CD<sub>2</sub>Cl<sub>2</sub>, 600 MHz): δ 13.86 (s, 2H, OH), 8.09 (m, 6H, ArH), 7.90 (d, 2H, ArH), 7.42 (dd, 2H, ArH), 6.99 (d, 2H, ArH), 1.39 (s, 18H, -C(CH<sub>3</sub>)<sub>3</sub>), <sup>13</sup>C {<sup>1</sup>H} NMR (CD<sub>2</sub>Cl<sub>2</sub>, 600 MHz): δ 158.50 (ArC), 157.59 (ArC), 152.36 (ArC), 142.05 (ArC), 139.49 (ArC), 129.67 (ArC), 128.90 (ArC), 123.29 (ArC), 120.20 (ArC), 119.27 (ArC), 118.37 (ArC), 118.28 (ArC), 34.56 (tbuC), 31.89 (tbuC). Elemental analysis for C<sub>30</sub>H<sub>32</sub>O<sub>2</sub>N<sub>2</sub> calculated: C 79.61, H 7.13, N 6.19; found C 79.63, H 7.25, N 6.22.

### Synthesis of Ni( $P^{t\text{-bu}}\text{dhbpy}$ ) **1**

The  $P^{t\text{-bu}}\text{dhbpy}$  ligand (250 mg, 0.552 mmol) was dissolved in ethanol (50 mL) in a round-bottom flask. Sodium acetate (0.095 g, 1.2 mmol) and nickel(II) chloride hexahydrate (0.131 g, 0.552 mmol) were added to the solution and stirred under air at room temperature. The reaction mixture was then brought to refluxing conditions (90 °C) for 4 hours. The resulting suspension was filtered and washed with diethyl ether to yield a dark orange solid. The solid was further purified by suspending it in brine (50 mL) and extracting with dichloromethane (3 x 50 mL). The organic fractions were combined, dried with anhydrous magnesium sulfate, and solvent was evaporated under reduced pressure to yield 0.264 g of **1** in 93.9% yield. <sup>1</sup>H NMR (CD<sub>2</sub>Cl<sub>2</sub>, 600 MHz): δ 8.08 (m, 2H, ArH), 7.95 (m, 2H, ArH), 7.70 (m, 2H, ArH), 7.31 (m, 2H, ArH), 7.01 (m, 2H, ArH), 1.36 (s, 18H, -C(CH<sub>3</sub>)<sub>3</sub>). Elemental analysis for C<sub>30</sub>H<sub>30</sub>NiO<sub>2</sub>N<sub>2</sub>: calculated: C 70.75, H 5.94, N 5.50; found C 70.70, H 6.03, N 5.47.

## Single Mass Analysis

Tolerance = 5.0 PPM / DBE: min = -1.5, max = 200.0

Element prediction: Off

Number of isotope peaks used for i-FIT = 9

Monoisotopic Mass, Even Electron Ions

448 formula(e) evaluated with 2 results within limits (up to 50 best isotopic matches for each mass)

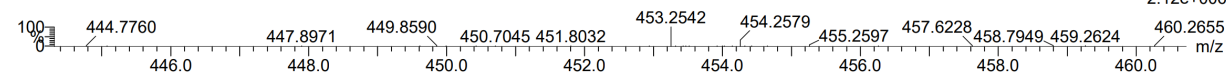
Elements Used:

C: 0-110 H: 0-120 N: 0-5 O: 0-6 Ni: 0-1

Shelby Hooe JMD-OH-01

MSL, School of Chemical Sciences, UIUC

Synapt2\_2156 32 (0.637) Cm (32-6:8x2.000)

1: TOF MS ES+  
2.12e+006Minimum: -1.5  
Maximum: 5.0 5.0 200.0

Mass	Calc. Mass	mDa	PPM	DBE	i-FIT	Norm	Conf (%)	Formula
453.2542	453.2542	0.0	0.0	15.5	251.5	0.000	100.00	C30 H33 N2 O2
	453.2542	0.0	0.0	8.5	262.4	10.941	0.00	C27 H41 N O Ni

Figure S1. ESI-MS results for  $P^{t\text{-bu}}\text{dhp}y(\text{H}_2)$  ligand.

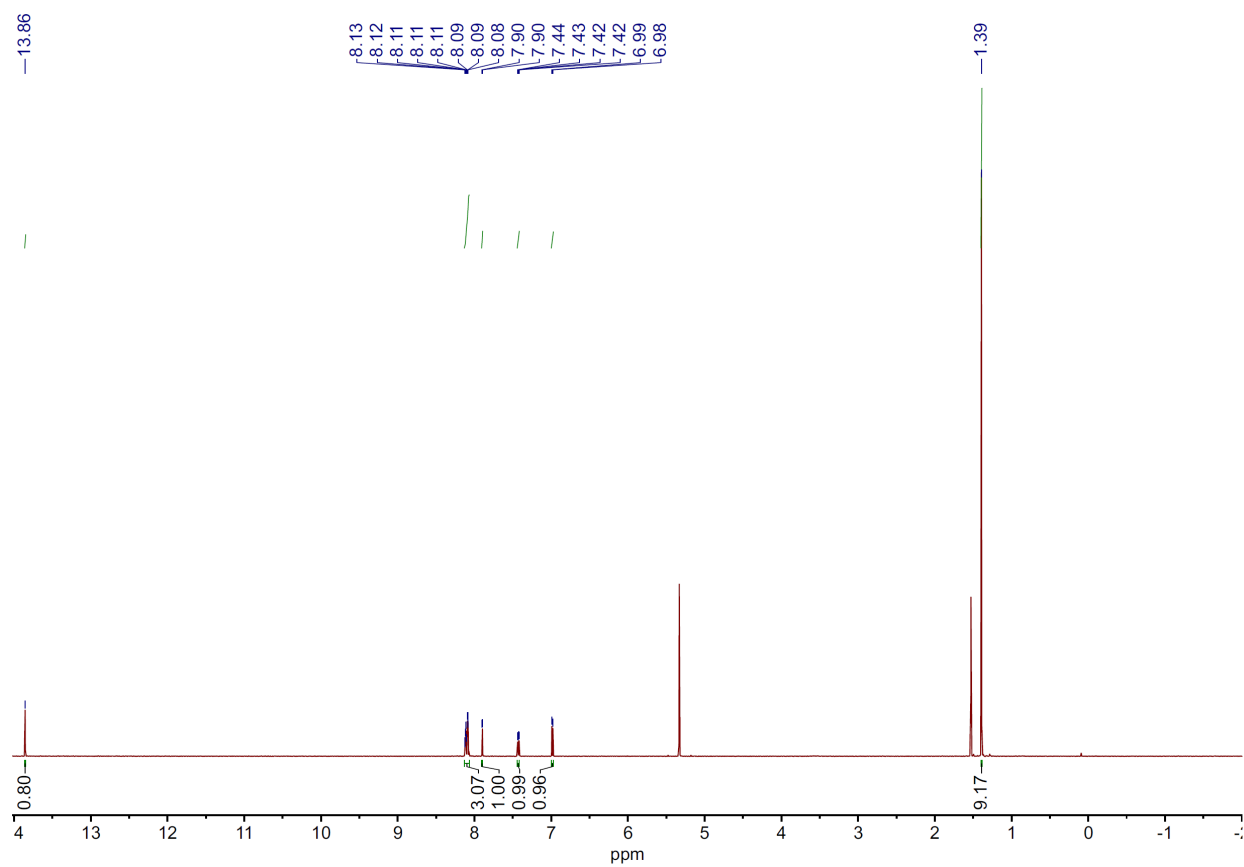


**Figure S2.**  $^1\text{H}$  NMR of  $p\text{-tbuhbpy}(\text{H}_2)$  ligand in  $\text{CD}_2\text{Cl}_2$ ; 600 MHz.

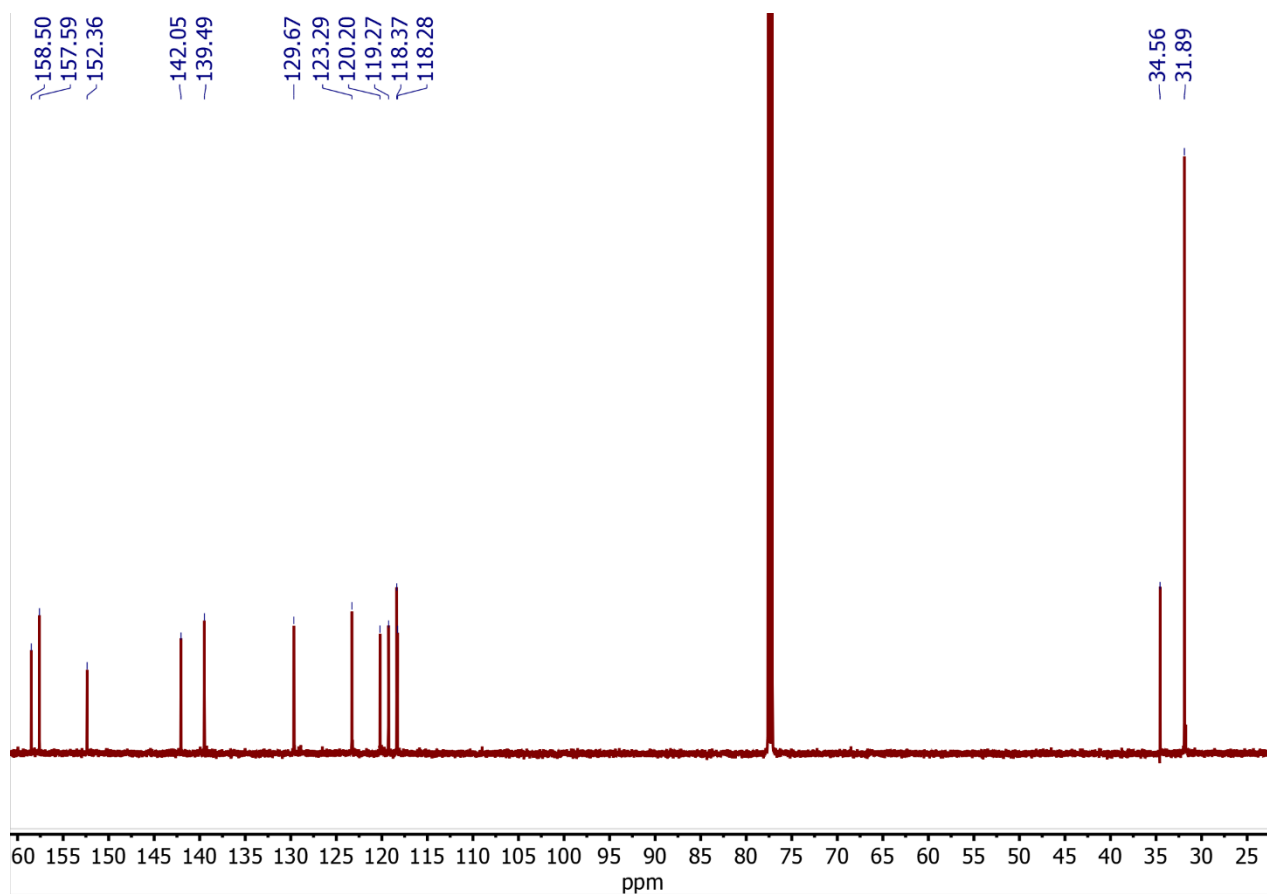


**Figure S3.**  $^{13}\text{C}\{^1\text{H}\}$  NMR of  $p\text{-}^{\text{t}}\text{buhbpy}(\text{H}_2)$  ligand in  $\text{CD}_2\text{Cl}_2$ ; 151 MHz.

### Elemental Composition Report

Page 1

#### Single Mass Analysis

Tolerance = 5.0 PPM / DBE: min = -1.5, max = 200.0

Element prediction: Off

Number of isotope peaks used for i-FIT = 9

Monoisotopic Mass, Odd and Even Electron Ions

504 formula(e) evaluated with 5 results within limits (up to 50 best isotopic matches for each mass)

Elements Used:

C: 0-110 H: 0-120 N: 0-5 O: 0-6 Ni: 0-1

Shelby Hooe JMD-Ni-02

MSL, School of Chemical Sciences, UIUC

Synapt2\_2155 23 (0.465) Cm (23:24-8x2.000)

1: TOF MS ES+  
2.49e+006



Minimum: -1.5  
Maximum: 5.0 5.0 200.0

Mass	Calc. Mass	mDa	PPM	DBE	i-FIT	Norm	Conf (%)	Formula
509.1741	509.1739	0.2	0.4	24.0	1671.2	0.947	38.80	C33 H23 N3 O3
	509.1753	-1.2	-2.4	23.5	1671.6	1.268	28.15	C35 H25 O4
	509.1766	-2.5	-4.9	28.5	1672.1	1.762	17.18	C36 H21 N4
	509.1726	1.5	2.9	17.5	1672.7	2.389	9.18	C28 H29 N5 O Ni
	509.1739	0.2	0.4	17.0	1673.0	2.704	6.69	C30 H31 N2 O2 Ni

**Figure S4.** ESI-MS results for  $\text{Ni}(p\text{-}^{\text{t}}\text{buhbpy}) \mathbf{1}$ .

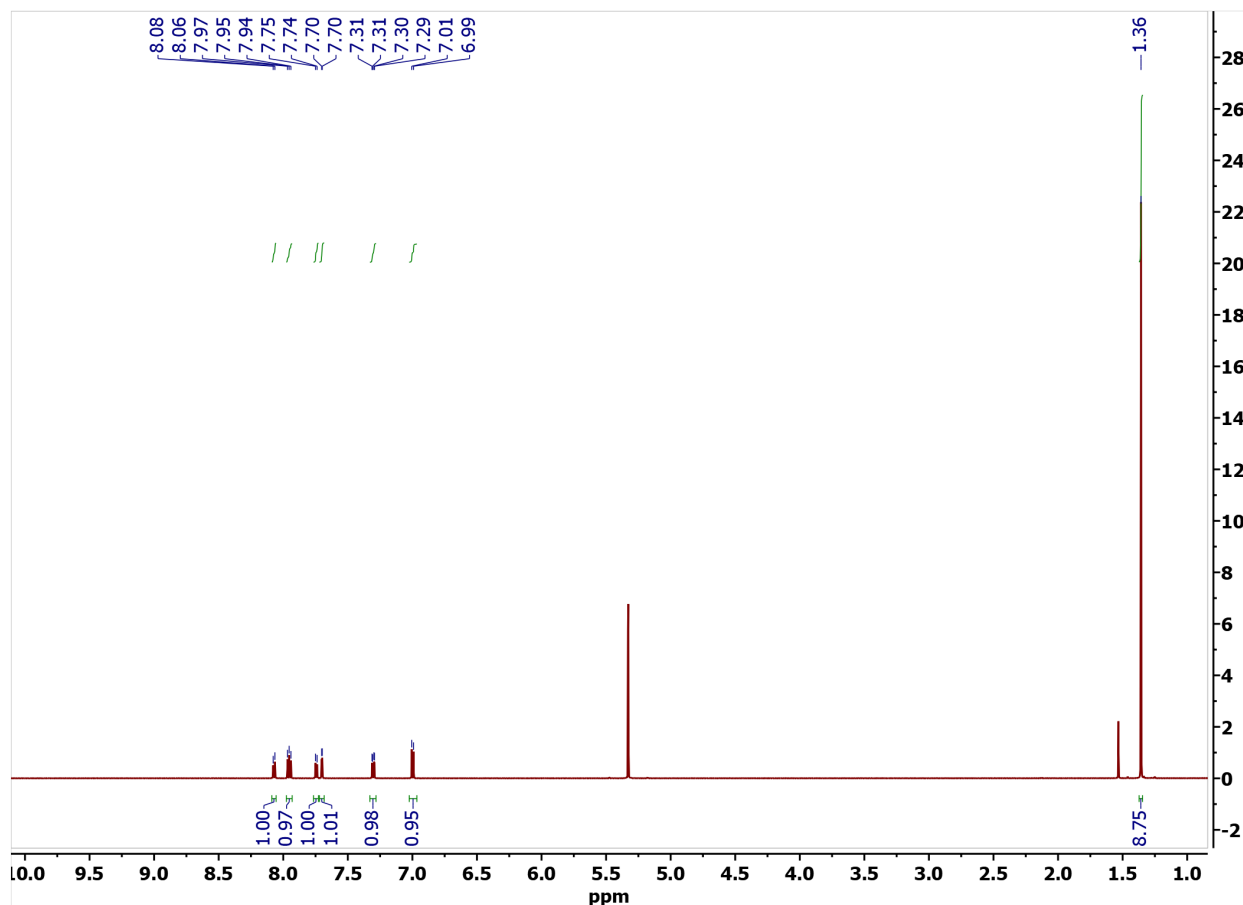


**Figure S5.**  $^1\text{H}$  NMR of  $\text{Ni}(\text{p-tbu-dhbp})$  **1** in  $\text{CD}_2\text{Cl}_2$ ; 600 MHz.

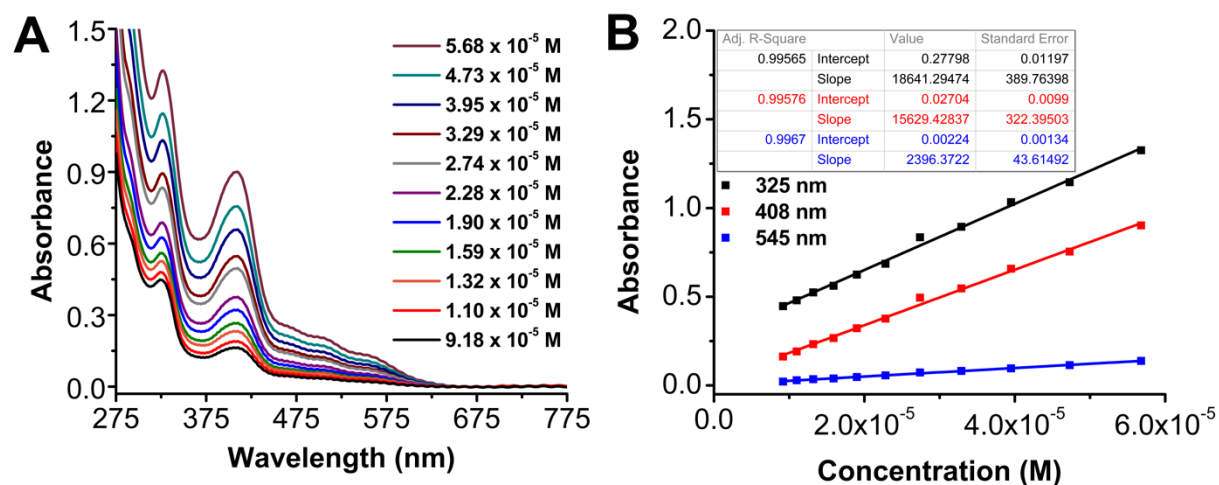


**Figure S6.** (A) UV-vis serial dilution absorbance data obtained from  $\text{Ni}(\text{p-tbu-dhbp})$  **1** in  $N,N$ -DMF solution. (B) Plot of absorbance versus concentration from data in (A) ( $\lambda_{\text{max}} = 325$  ( $18600 \text{ M}^{-1}\text{cm}^{-1}$ ),  $408$  ( $15600 \text{ M}^{-1}\text{cm}^{-1}$ ), and  $545 \text{ nm}$  ( $2400 \text{ M}^{-1}\text{cm}^{-1}$ ). Conditions: varying concentration; quartz cell with 1 cm pathlength.

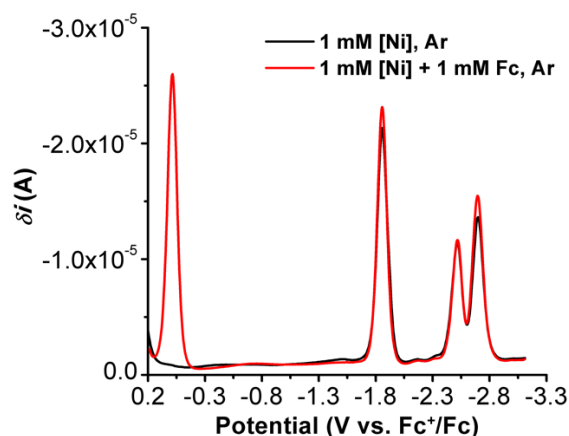


**Figure S7.** DPVs of Ni(<sup>p-tbu</sup>dhbpy) **1** under Ar saturation with (red) and without (black) 1 mM ferrocene present. Conditions: 1.0 mM analyte, 0.1 M TBAPF<sub>6</sub>/*N,N*-DMF; glassy carbon working electrode, glassy carbon counter electrode, Ag/AgCl pseudoreference electrode,  $\Delta E = 0.025$  V, modulation time 0.01 s, interval time 0.1 s, scan rate 50.354 mV/s. Referenced to internal ferrocene standard.

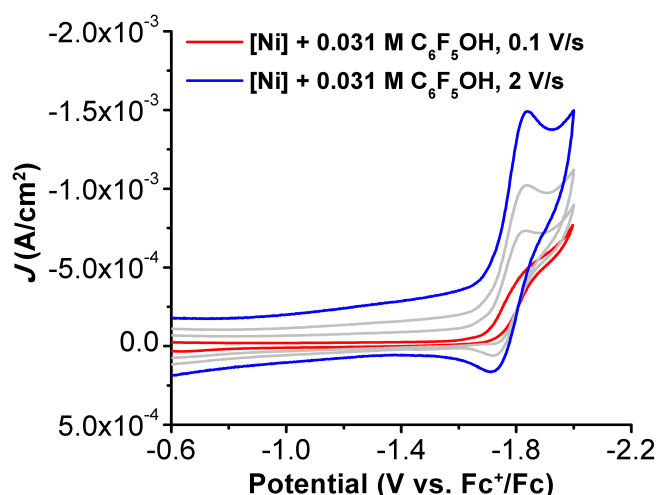


**Figure S8.** CVs of Ni(<sup>p-tbu</sup>dhbpy) **1** at variable scan rates in the presence of 0.031 M C<sub>6</sub>F<sub>5</sub>OH ranging from 0.1 to 2 V/s used to obtain  $K_{C_6F_5OH}$ . Conditions: 1.0 mM analyte, 0.1 M TBAPF<sub>6</sub>/*N,N*-DMF; glassy carbon working electrode, glassy carbon counter electrode, Ag/AgCl pseudoreference electrode; varied scan rate; referenced to internal ferrocene standard.

The equilibrium binding constant for C<sub>6</sub>F<sub>5</sub>OH in a 1:1 ratio with complex **1** was electrochemically determined as previously reported.<sup>1</sup> A scan rate of 2 V/s was necessary to recover reversibility and the  $E_{1/2}$  of the first reduction feature from **Figure S9** at 2 V/s was used ( $E_{1/2} = -1.86$  V vs. Fc<sup>+</sup>/Fc).

$$K_{C_6F_5OH} = \frac{e^{(f \cdot \Delta E)} - 1}{[C_6F_5OH]} = 695 \text{ M}^{-1}$$

Where  $f = F/RT = 38.94 \text{ V}^{-1}$ ,  $\Delta E = E_{1/2,C_6F_5OH} - E_{1/2} = 0.080 \text{ V}$ , and  $[C_6F_5OH] = 0.031 \text{ M}$ .

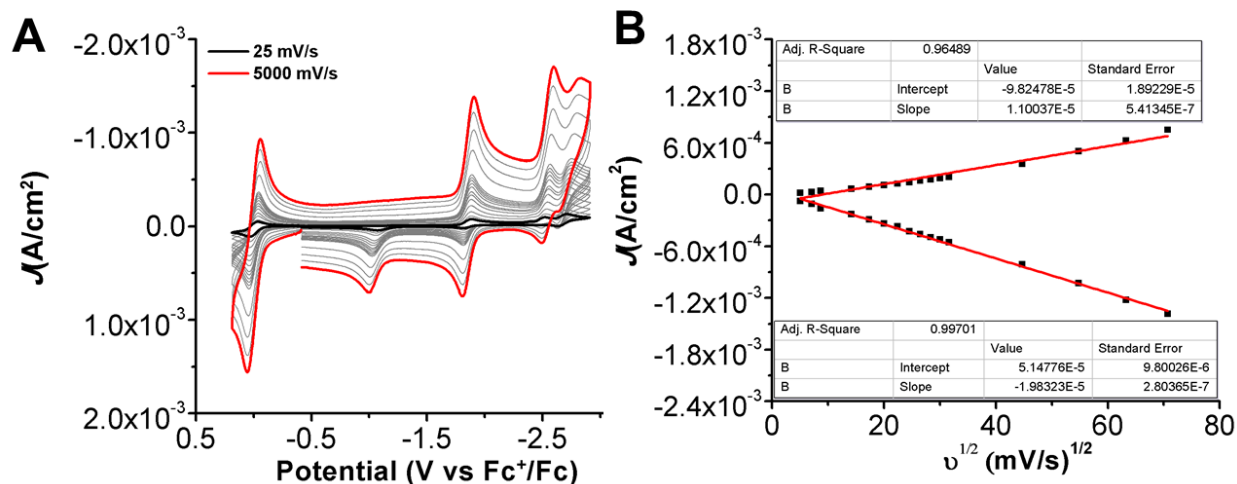


**Figure S9.** (A) CVs of Ni(<sup>p-tbu</sup>dhbpy) **1** at variable scan rates ranging from 25 (black) to 5000 (red) mV/s, obtained under Ar saturation conditions. (B) Linear Fit of variable scan rate data from (A) demonstrating that Ni(<sup>p-tbu</sup>dhbpy) **1** shows a diffusion-limited current response. The data in (B) was obtained from the reversible redox feature at  $-1.84$  V vs Fc<sup>+</sup>/Fc. Conditions: 1.0 mM analyte, 0.1 M TBAPF<sub>6</sub>/*N,N*-DMF; glassy carbon working electrode, glassy carbon counter electrode, Ag/AgCl pseudoreference electrode; varied scan rate; referenced to internal ferrocene standard.

Evaluation of homogenous electrochemical processes described by the Randles-Sevcik equation:<sup>20</sup>

$$i_p = 0.446nFAC^0 \left( \frac{nFvD_0}{RT} \right)^{0.5}$$

Where  $i_p$  is the peak Faradaic current,  $n$  is the number of electrons transferred in the redox process,  $F$  is Faraday's constant,  $A$  is the electrode surface area,  $C^0$  is the concentration of analyte in the bulk solution,  $v$  is the scan rate, and  $D_0$  is the diffusion coefficient of the analyte.

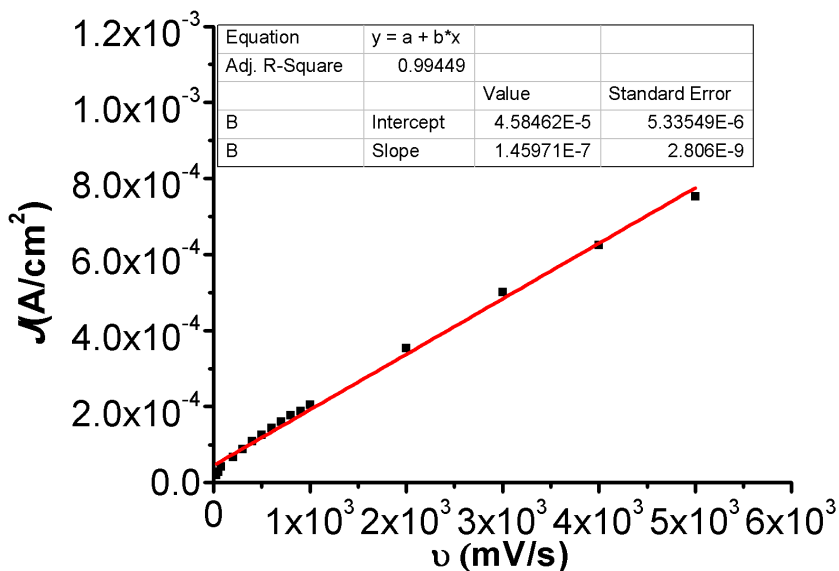


**Figure S10.** Linear fit of variable scan rate data from **Figure S9 (A)**. The data was obtained from the oxidation wave of the irreversible redox feature at  $-1.81$  V vs  $\text{Fc}^+/\text{Fc}$ . Conditions: 1.0 mM analyte, 0.1 M TBAPF<sub>6</sub>/DMF; glassy carbon working electrode, glassy carbon counter electrode, Ag/AgCl pseudoreference electrode; varied scan rate; referenced to internal ferrocene standard.

Evaluation of heterogenous electrochemical processes described by:<sup>20</sup>

$$i_p = \frac{n^2 F^2}{4RT} v A \Gamma^*$$

Where  $i_p$  is the peak Faradaic current,  $n$  is the number of electrons transferred in the redox process,  $F$  is Faraday's constant,  $R$  is the ideal gas constant,  $T$  is the temperature,  $A$  is the electrode surface area,  $v$  is the scan rate, and  $\Gamma^*$  represents the surface coverage of the adsorbed species.

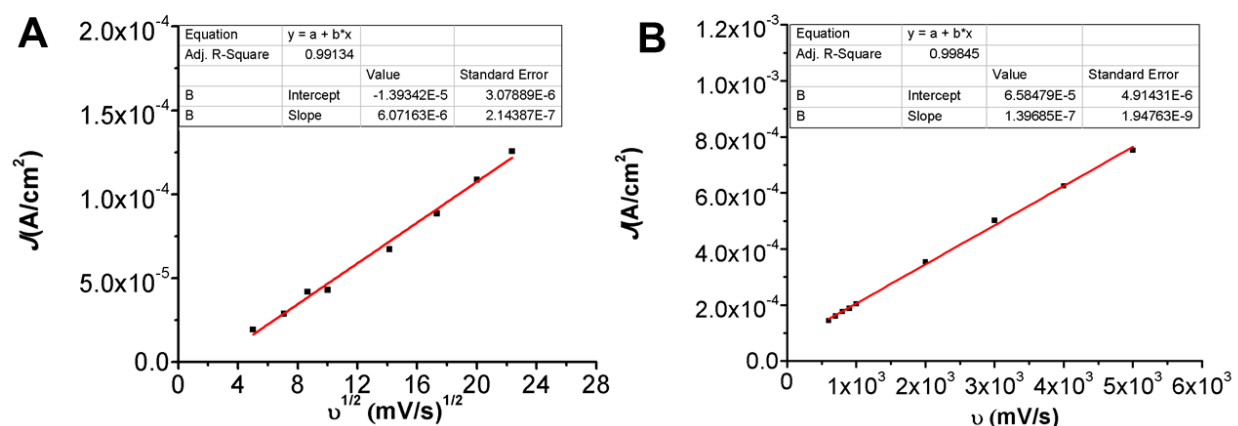


**Figure S11.** Comparison of linear fits of variable scan rate data from **Figure S9** at  $E_p = -1.81$  V vs.  $\text{Fc}^+/\text{Fc}$  from (A) 25-500 mV/s and (B) from 600-5000 mV/s to demonstrate adsorptive process above 500 mV/s. Conditions: 1.0 mM analyte, 0.1 M TBAPF<sub>6</sub>/*N,N*-DMF; glassy carbon working electrode, glassy carbon counter electrode, Ag/AgCl pseudoreference electrode; varied scan rate; referenced to internal ferrocene standard.

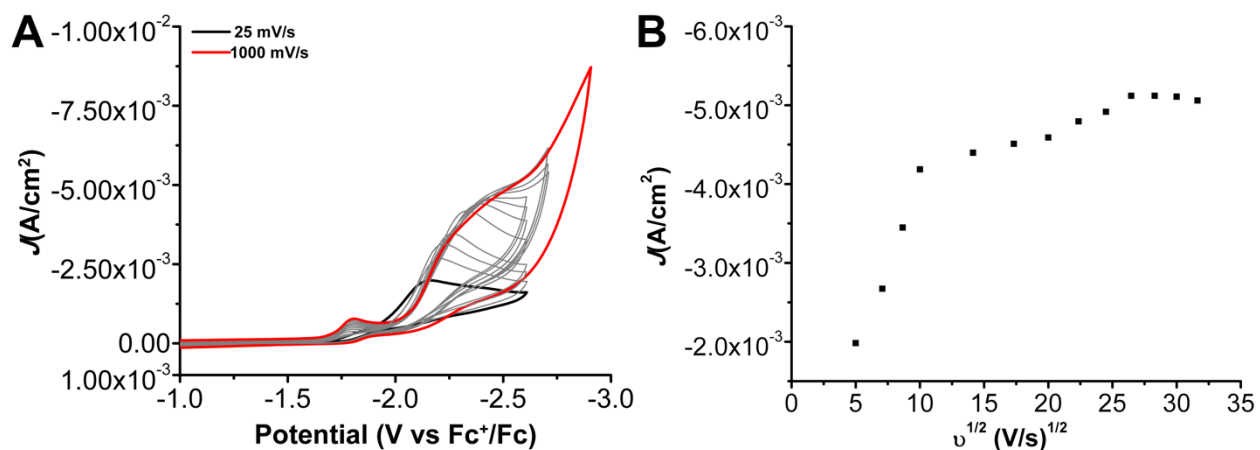


**Figure S12.** (A) CVs of Ni(<sup>p-tbu</sup>dhbpy) **1** at variable scan rates ranging from 25 mV/s (black) to 1000 mV/s (red), obtained under Ar saturation conditions with 0.033M C<sub>6</sub>F<sub>5</sub>OH. (B) Linear fit of variable scan rate data from (A). The data in (B) was obtained from the redox feature at -2.33 V vs Fc<sup>+</sup>/Fc. Conditions: 1.0 mM analyte, 0.1 M TBAPF<sub>6</sub>/DMF; glassy carbon working electrode, glassy carbon counter electrode, Ag/AgCl pseudoreference electrode; varied scan rate; referenced to internal ferrocene standard.

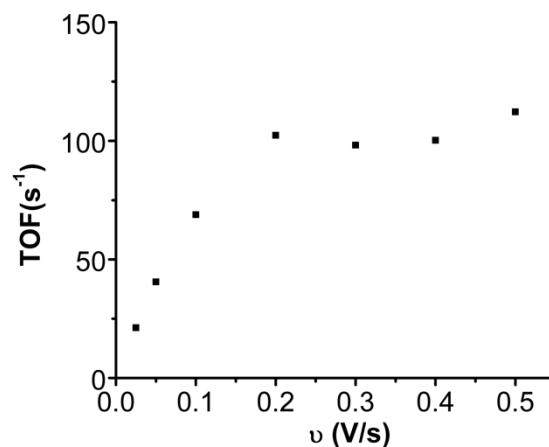


**Figure S13.** Plot of TOF versus scan rate for Ni(<sup>p-tbu</sup>dhbpy) **1** with 0.033 M C<sub>6</sub>F<sub>5</sub>OH. Calculation of TOF<sub>max</sub> (adapted<sup>21</sup>):

$$TOF_{max} = 0.1992 \frac{n_p^3}{n_{cat}^2} \frac{Fv}{RT} \left( \frac{i_{cat}}{i_p} \right)^2$$

Where  $n_p$  is the number of electrons transferred under Faradaic, or non-catalytic, conditions,  $n_{cat}$  is the number of electrons transferred under catalytic conditions,  $F$  is Faraday's constant,  $v$  is the scan rate,  $R$  is the ideal gas constant, and  $T$  is the temperature. The values for  $i_{cat}$  and  $i_p$  were both selected from the peak current at the second wave under catalytic and Faradaic conditions, respectively.

Under catalytic conditions, the current density did not increase linearly with the square root of the scan rate at the second reduction feature,  $E_p = -2.33$  V vs Fc<sup>+</sup>/Fc (**Figure S12**), with the peak current plateauing at scan rates above 500 mV/s. Since adsorption was suggested by variable scan rate data above 500 mV/s, TOF<sub>max</sub> was calculated for each scan rate from 200-500 mV/s as a conservative estimate (**Table S1**).

**Table S1.** TOF<sub>max</sub> at scan rates from 0.2-0.5 V/s of Ni(<sup>p-tbu</sup>dhbpy) **1** calculated using data in **Figure S12** and **Figure S13**.

Scan Rate (V/s)	$\frac{i_{cat}}{i_p}$	TOF <sub>max</sub> (s <sup>-1</sup> )
0.2	16.2	102
0.3	13.0	98.3
0.4	11.4	100
0.5	10.8	112

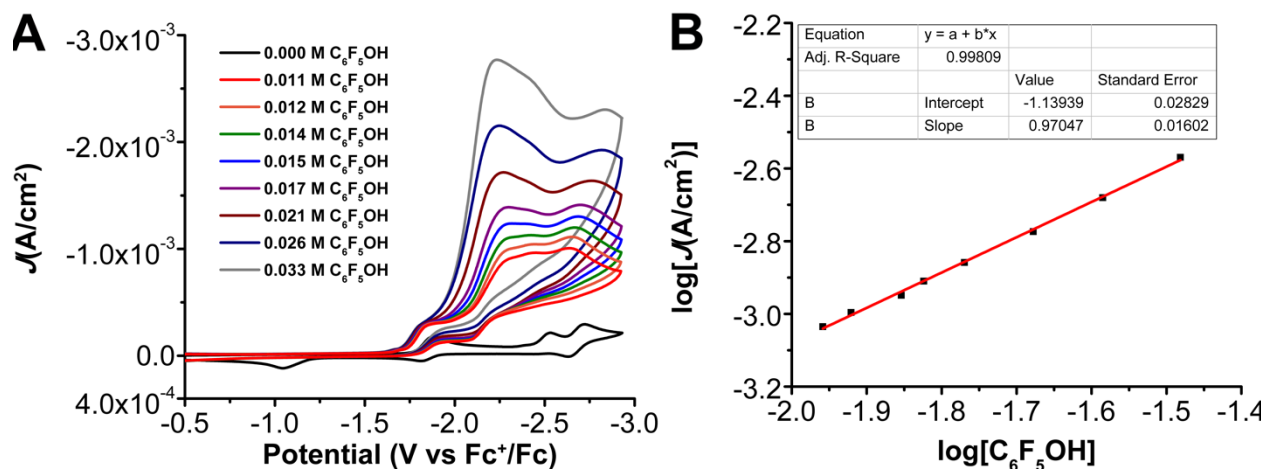


**Figure S14.** (A) CVs of C<sub>6</sub>F<sub>5</sub>OH at variable concentrations, obtained under Ar saturation with 1.0 mM Ni(p<sup>tbu</sup>dhbpy) **1**. Conditions: 0.1 M TBAPF<sub>6</sub>/N,N-DMF; glassy carbon working electrode, glassy carbon counter electrode, Ag/AgCl pseudoreference electrode; 100 mV/s scan rate; referenced to internal ferrocene standard. (B) Log-log plot of data at in (A) -2.24 V vs Fc<sup>+</sup>/Fc.

Calculation of rate order adapted from Sathrum and Kubiak, 2011<sup>22</sup>

$$i_{cat} = n_{cat}FA[cat](Dk_{cat}[Q]^y)^{1/2}$$

Where  $i_{cat}$  is the catalytic current,  $n_{cat}$  is the number of electrons involved in the catalytic process,  $F$  is Faraday's constant,  $A$  is the electrode area,  $[cat]$  is the concentration of the catalyst,  $D$  is the diffusion coefficient of the catalyst,  $k_{cat}$  is the catalytic rate,  $[Q]$  is the substrate concentration, and  $y$  is the rate order with respect to  $Q$ .

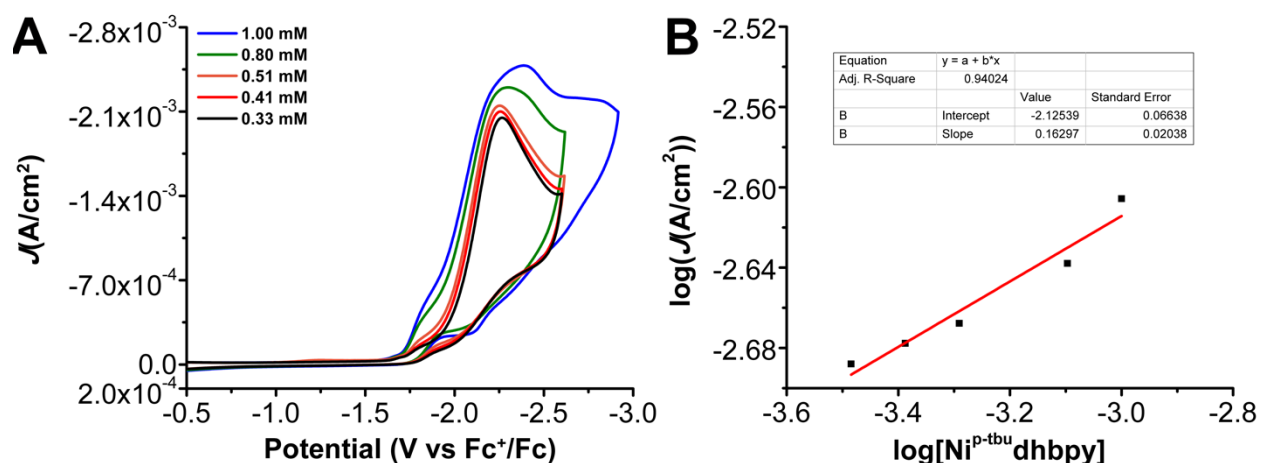


**Figure S15.** (A) CVs of variable Ni(p-tbuhbpy) **1** concentrations with 0.033 M C<sub>6</sub>F<sub>5</sub>OH obtained under Ar saturation. Conditions: 1.0 mM analyte, 0.1 M TBAPF<sub>6</sub>/DMF; glassy carbon working electrode, glassy carbon counter electrode, Ag/AgCl pseudoreference electrode; varied scan rate; referenced to internal ferrocene standard. (B) Log-log plot from data obtained from (A) at -2.23 V vs Fc<sup>+</sup>/Fc.

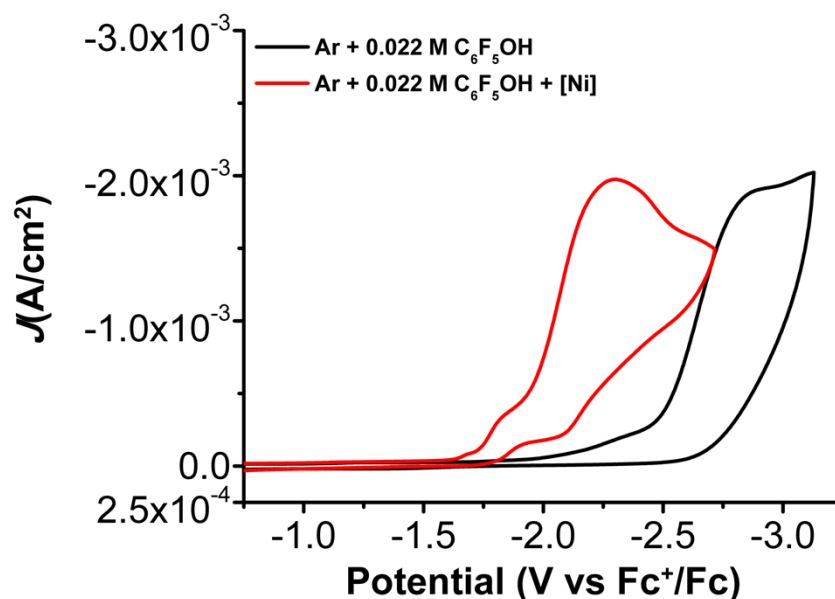


**Figure S16.** Control CV data comparing 0.022 M C<sub>6</sub>F<sub>5</sub>OH under Ar saturation conditions with (red) and without (black) 1.0 mM Ni(p-tbuhbpy) **1**. Conditions: 0.1 M TBAPF<sub>6</sub>/*N,N*-DMF; glassy carbon working electrode, glassy carbon counter electrode, Ag/AgCl pseudoreference electrode; 100 mV/s scan rate; referenced to internal ferrocene standard. [Ni] = 1.0 mM Ni(p-tbuhbpy) **1**.

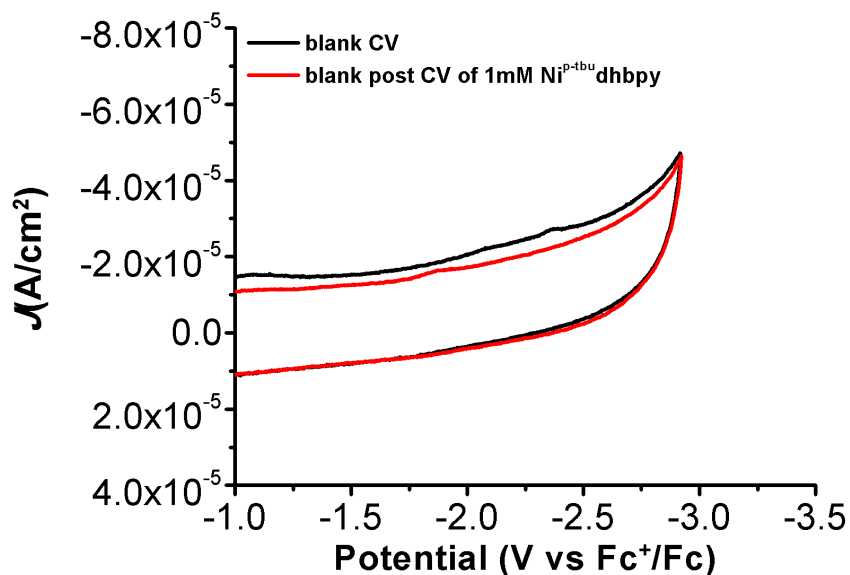


**Figure S17.** Rinse test CV data comparing a blank CV under Ar saturation conditions (black) with a blank CV taken immediately after a CV in a solution of 1.0 mM Ni(<sup>p-tbu</sup>dhbpy) **1** (red). Conditions: 0.1 M TBAPF<sub>6</sub>/*N,N*-DMF; glassy carbon working electrode, glassy carbon counter electrode, Ag/AgCl pseudoreference electrode; 100 mV/s scan rate; referenced to internal ferrocene standard.

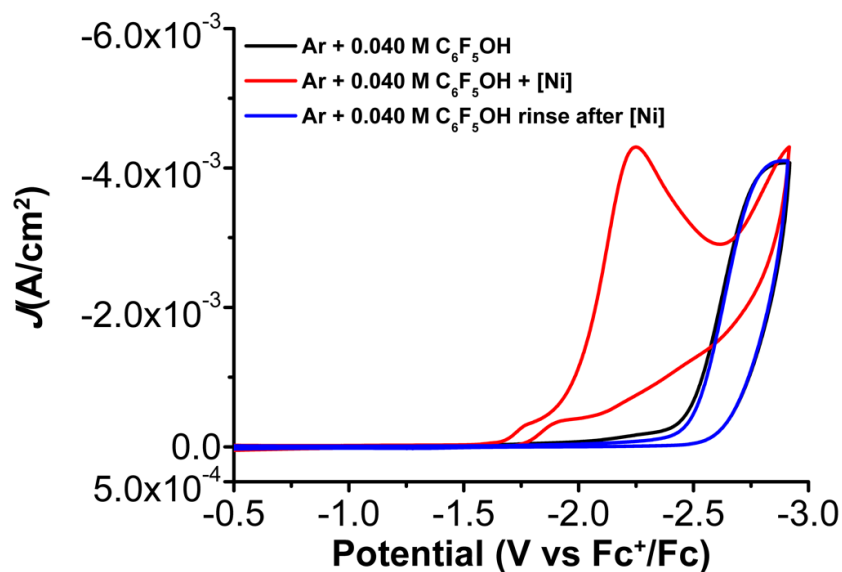


**Figure S18.** Rinse test CV data comparing a CV of Ni(<sup>p-tbu</sup>dhbpy) **1** with 0.04 M C<sub>6</sub>F<sub>5</sub>OH (red), a blank CV taken immediately after a CV in a solution of 1.0 mM Ni(<sup>p-tbu</sup>dhbpy) **1** with 0.04 M C<sub>6</sub>F<sub>5</sub>OH (blue), and a blank CV of 0.04 M C<sub>6</sub>F<sub>5</sub>OH (black) under Ar saturation conditions. Conditions: 0.1 M TBAPF<sub>6</sub>/*N,N*-DMF; glassy carbon working electrode, glassy carbon counter electrode, Ag/AgCl pseudoreference electrode; 100 mV/s scan rate; referenced to internal ferrocene standard.

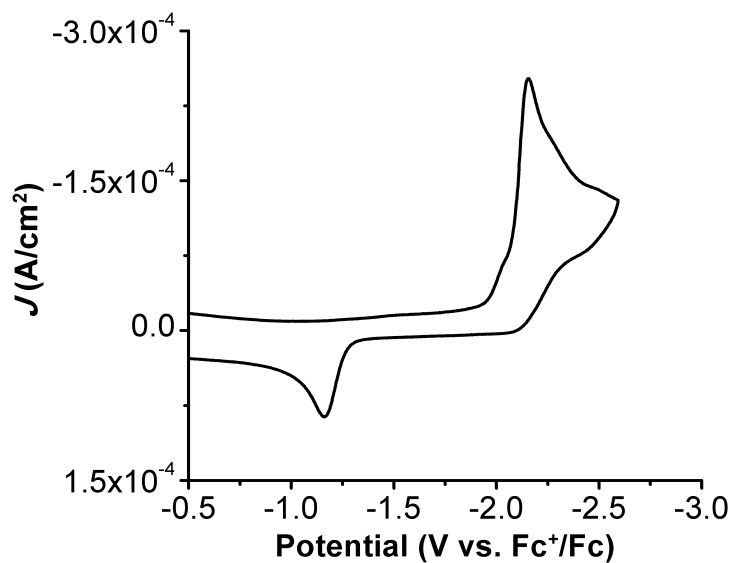


**Figure S19.** CV of  $p\text{-tbuhbpy}(\text{H}_2)$  ligand under Ar saturation. Conditions: 1.0 mM analyte, 0.1 M TBAPF<sub>6</sub>/DMF; glassy carbon working electrode, glassy carbon counter electrode, Ag/AgCl pseudoreference electrode; 100 mV/s scan rate; referenced to internal ferrocene standard.

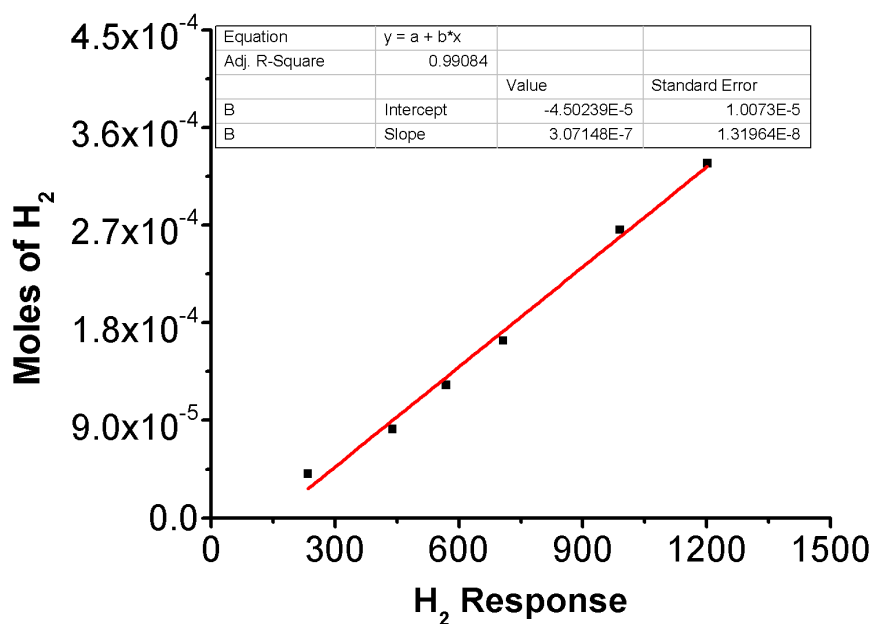


**Figure S20.** Gas chromatogram calibration curve for the quantification of H<sub>2</sub> in CPE experiments.

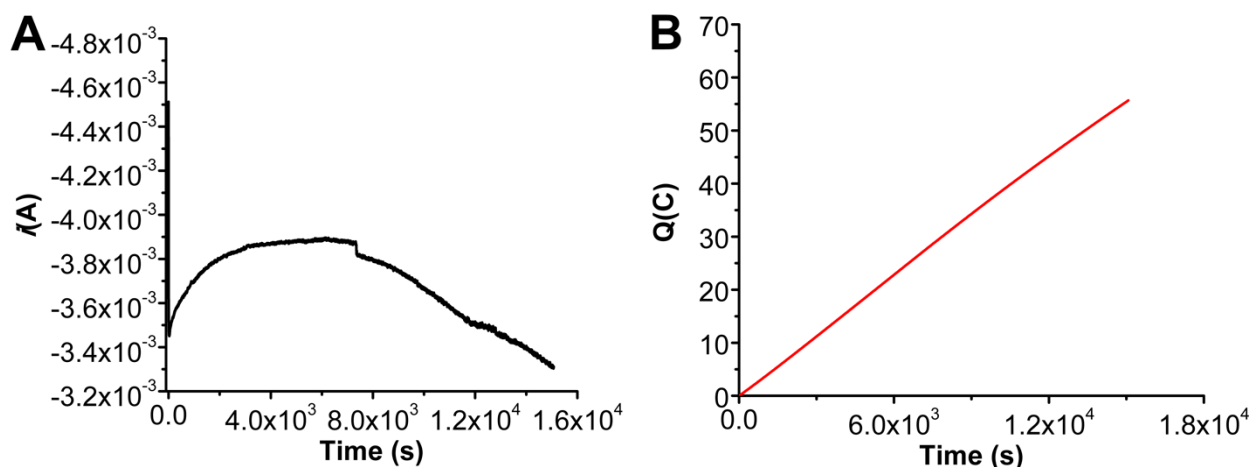


**Figure S21.** (A) Current versus time trace from bulk electrolysis experiment. (B) Charge passed versus time for the bulk electrolysis experiment shown in (A). Conditions were 1.0 mM Ni( $P^{t\text{bu}}\text{dhbpy}$ ) **1** under an Ar atmosphere with 0.05 M  $\text{C}_6\text{F}_5\text{OH}$  at  $-1.9$  V vs  $\text{Fc}^+/\text{Fc}$  in 0.1 M  $\text{TBAPF}_6/N,N\text{-DMF}$ ; working electrode was a glassy carbon rod, counter electrode was a graphite rod, and the reference was a nonaqueous  $\text{Ag}/\text{AgCl}$  pseudoreference electrode; 0.075 M  $\text{Fc}$  was used as sacrificial oxidant.

**Table S2.** Results from CPE experiment in **Figure S19**, black.

Time (s)	Charge (coulombs)	moles ( $e^-$ )	Moles of $\text{H}_2$	$\text{FE}_{\text{H}_2}$	TON
7400	28.3	2.93E-04	1.53E-04	104.25	5.09
9800	37.4	3.88E-04	2.01E-04	103.92	6.70
12800	48.3	5.01E-04	2.02E-04	80.81	6.73
15000	55.7	5.77E-04	2.95E-04	102.11	9.81
15000	55.7	5.77E-04	2.81E-04	97.45	9.36
15000	55.7	5.77E-04	2.42E-04	83.79	8.05

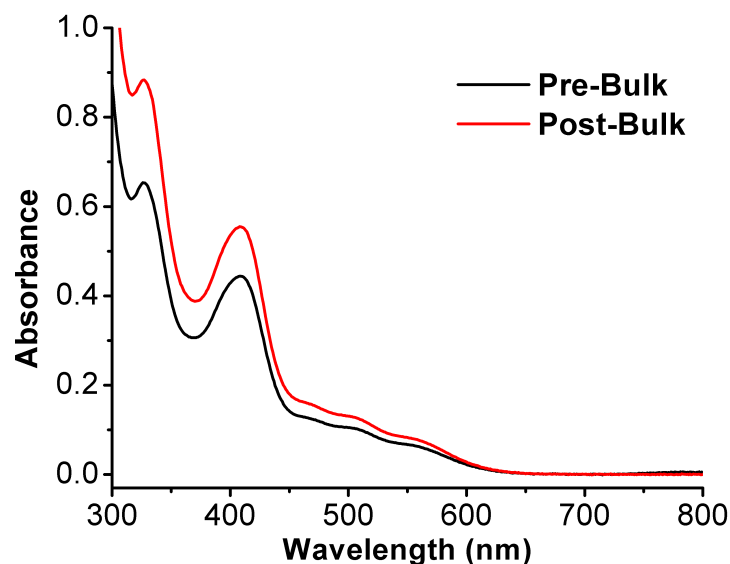


**Figure S22.** UV-vis spectra of pre- (black trace) and post-bulk (red trace) solutions after dilution. The increase in absorbance is attributed to the crossover of ferrocene and ferrocenium from the counter electrode chamber through the glass frit. Conditions: 0.05 mL CPE solution in 2.95 mL 0.1 M TBAPF<sub>6</sub>/N,N-DMF; quartz cell with 1 cm pathlength; CPE conditions: 1.0 mM Ni(P<sup>tbu</sup>dhbpy), 0.05 M C<sub>6</sub>F<sub>5</sub>OH, -1.9 V vs. Fc<sup>+</sup>/Fc in 0.1 M TBAPF<sub>6</sub>/N,N-DMF; Ar atmosphere, graphite rod working electrode, graphite rod counter electrode, with nonaqueous Ag/AgCl pseudoreference electrode; 0.075 M Fc was used as a sacrificial oxidant.

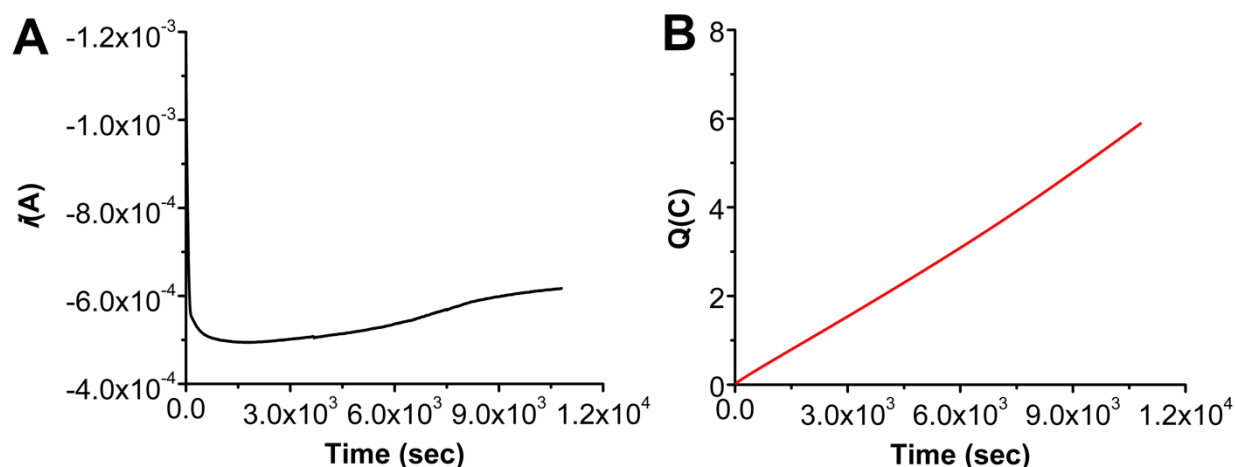


**Figure S23.** (A) Current versus time trace from rinse test post bulk electrolysis experiment in **Figure S21**. (B) Charge passed versus time for the bulk electrolysis experiment shown in (A). Conditions were 0.05 M C<sub>6</sub>F<sub>5</sub>OH under an Ar atmosphere at -1.9 V vs Fc<sup>+</sup>/Fc in 0.1 M TBAPF<sub>6</sub>/N,N-DMF; working electrode was a glassy carbon rod, counter electrode was a graphite rod, and the reference was a nonaqueous Ag/AgCl pseudoreference electrode; 0.075 M Fc was used as sacrificial oxidant.

**Table S3.** Results from CPE experiment in **Figure S23**, black.

Time (s)	Charge (coulombs)	moles (e-)	Moles of H <sub>2</sub>	FE <sub>H2</sub>	TON
3734	1.87	1.94E-05	Below limit	Below limit	Below limit
7492	3.92	4.06E-05	5.05E-06	24.88	0.17
10950	5.88	6.09E-05	1.94E-05	63.63	0.65
10950	5.88	6.09E-05	2.04E-05	67.04	0.68

\*Note that in order for the amount of H<sub>2</sub> to be detected, the GC injection volume was increased from 50  $\mu$ L to 100  $\mu$ L. To account for this, the calibration curve was adjusted such that the number of moles of H<sub>2</sub> corresponding to the GC response is doubled. This produced a new calibration curve with a slope of  $1.54\text{E-}7 \pm 7\text{E-}9$  and y-intercept of  $-2.25\text{E-}5 \pm 5\text{E-}6$ .

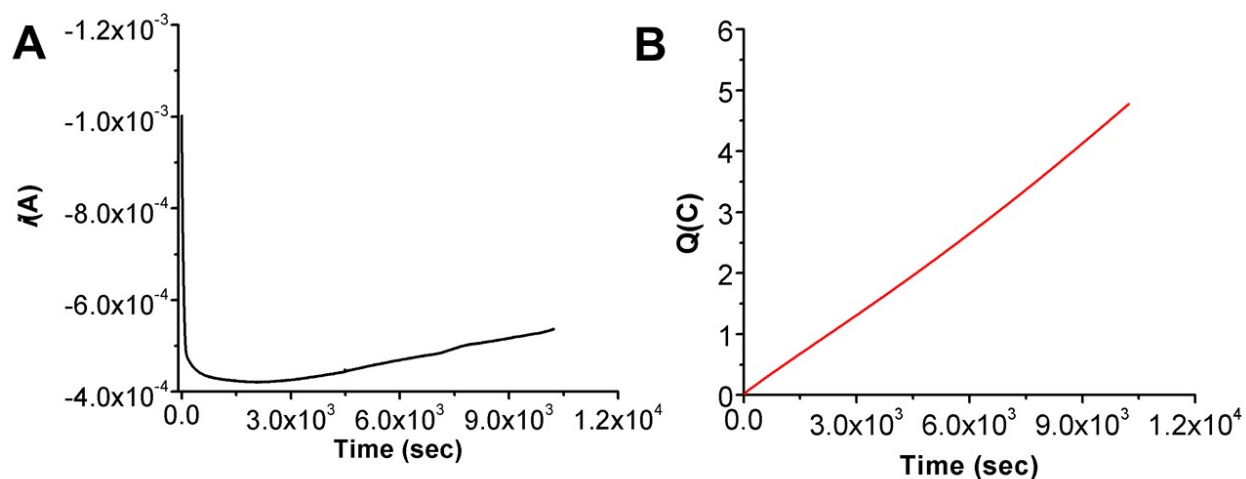


**Figure S24.** (A) Current versus time trace from control bulk electrolysis. (B) Charge passed versus time for the bulk electrolysis experiment shown in (A). Conditions were 0.05 M C<sub>6</sub>F<sub>5</sub>OH under an Ar atmosphere at  $-1.9$  V vs Fc<sup>+</sup>/Fc in 0.1 M TBAPF<sub>6</sub>/*N,N*-DMF; working electrode was a glassy carbon rod, counter electrode was a graphite rod, and the reference was a nonaqueous Ag/AgCl pseudoreference electrode; 0.075 M Fc was used as sacrificial oxidant.

**Table S4.** Results from CPE experiment in **Figure S24**, black.

<b>Time (s)</b>	<b>Charge (coulombs)</b>	<b>moles (e-)</b>	<b>Moles of H<sub>2</sub></b>	<b>FE<sub>H2</sub></b>	<b>TON</b>
4500	1.98	2.05E-05	Below LOQ	Below LOQ	Below LOQ
8150	3.69	3.83E-05	Below LOQ	Below LOQ	Below LOQ
10230	4.78	4.95E-05	Below LOQ	Below LOQ	Below LOQ
10230	4.78	4.95E-05	Below LOQ	Below LOQ	Below LOQ
10230	4.78	4.95E-05	Below LOQ	Below LOQ	Below LOQ

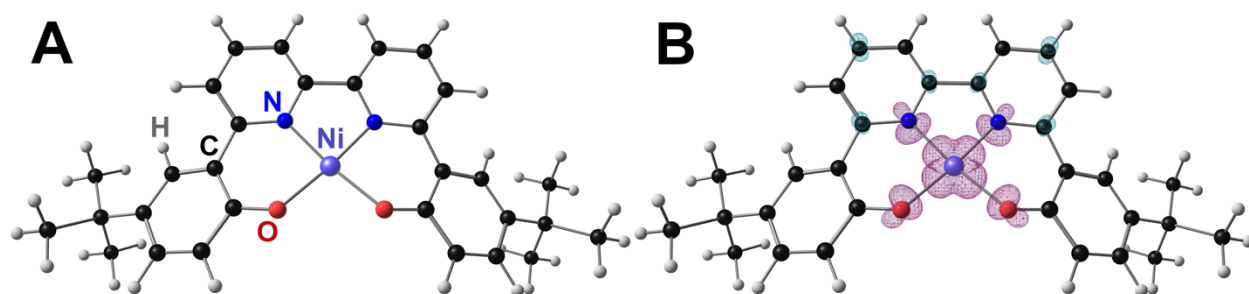


**Figure S25.** A computationally determined structure of one-electron reduced  $[\text{Ni}(\text{p-tbu-dhbpy})]^{1-}$  (A) and corresponding spin density plot showing localization on the Ni center consistent with a change in formal oxidation state from Ni(II) to Ni(I) (B).

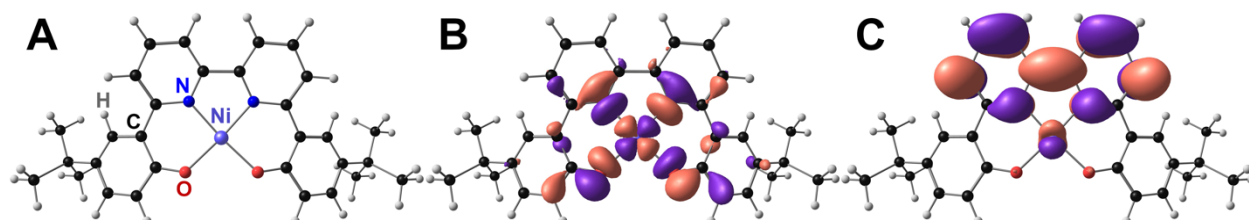


**Figure S26.** Structure of one-electron reduced  $[\text{Ni}(\text{p-tbu-dhbpy})]^{1-}$  (A) and corresponding KS orbital plots showing localization on the Ni center consistent with a change in formal oxidation state from Ni(II) to Ni(I) in the SOMO (B) and a bpy-based LUMO (C).

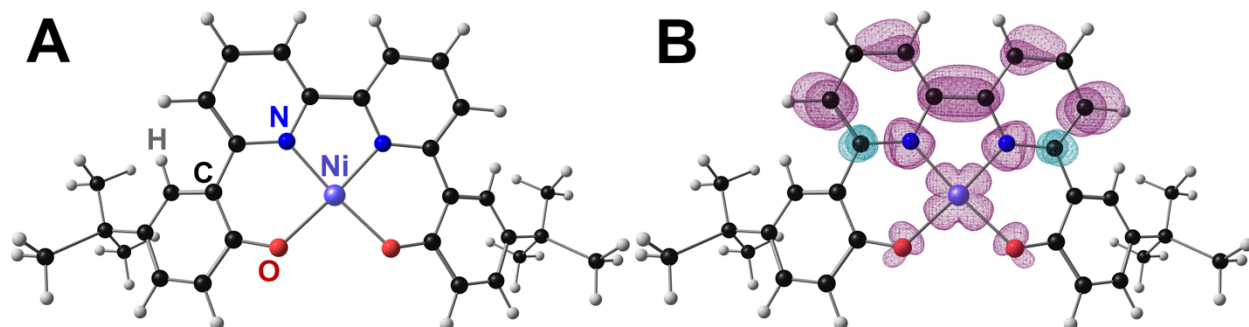


**Figure S27.** A computationally determined structure of two-electron reduced  $[\text{Ni}(\text{p-tbu-dhbpy})]^{2-}$  (A) and corresponding spin density plot showing localization of the second reduction on the bpy fragment of the ligand backbone (B). Compare to **Figure S22**.

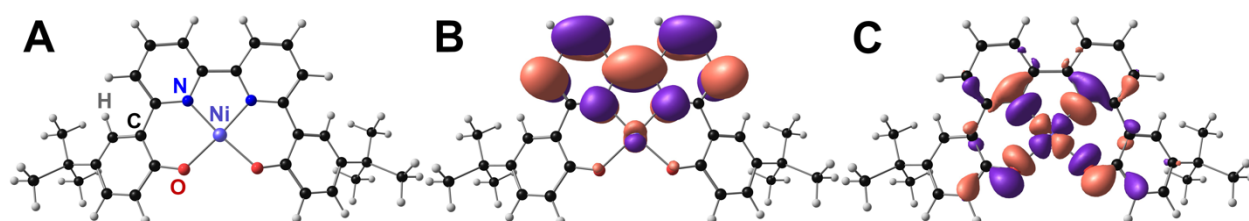


**Figure S28.** Structure of one-electron reduced  $[\text{Ni}(\text{p-tbu-dhbpy})]^{1-}$  (A) and corresponding KS orbital plots showing localization on the Ni center consistent with a bpy-based SOMO (B) and a Ni-based SOMO-1 consistent with a Ni(I) formal oxidation state (C). Compare to **Figure S23**.

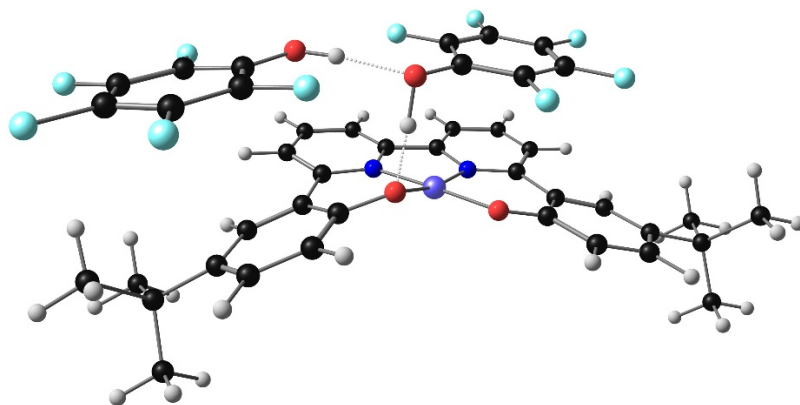


**Figure S29.** A computationally determined structure of  $[\text{Ni}(\text{p-}^{\text{t}}\text{bu-dhbp})(\text{C}_6\text{F}_5\text{OH})_2]^0$  as a stable bis- $\text{C}_6\text{F}_5\text{OH}$  adduct with a hydrogen-bonding chain. C = black; H = white; N = blue; O = red; F = turquoise; Ni = purple.

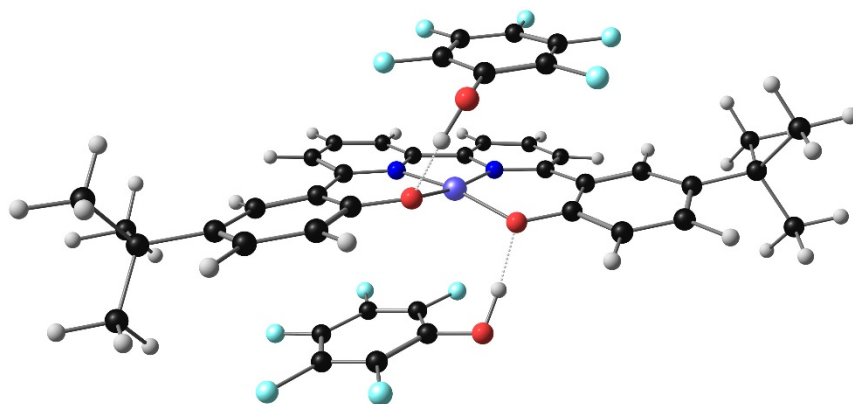
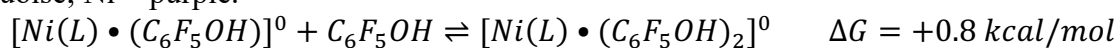


**Figure S30.** A computationally determined structure of  $[\text{Ni}(\text{p-}^{\text{t}}\text{bu-dhbp})(\text{C}_6\text{F}_5\text{OH})_2]^0$  as a stable bis- $\text{C}_6\text{F}_5\text{OH}$  adduct with hydrogen-bonding to both ligand O atoms. C = black; H = white; N = blue; O = red; F = turquoise; Ni = purple.

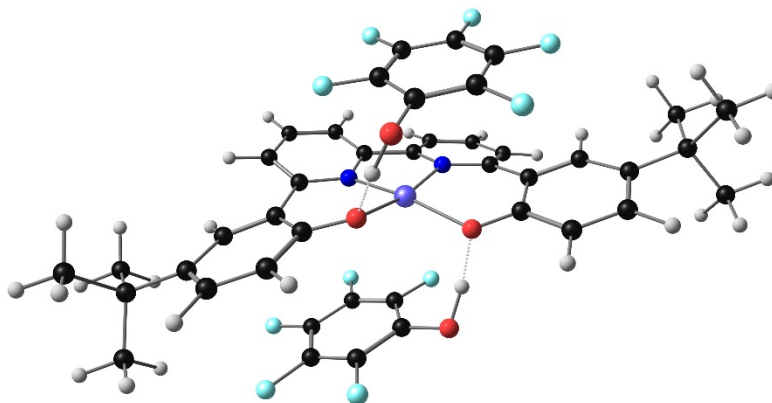
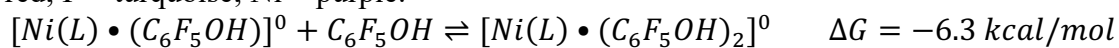
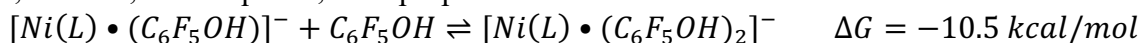


**Figure S31.** A computationally determined structure of  $[\text{Ni}(\text{p-}^{\text{t}}\text{bu-dhbp})(\text{C}_6\text{F}_5\text{OH})_2]^{1-}$  as a stable bis- $\text{C}_6\text{F}_5\text{OH}$  adduct with hydrogen-bonding to both ligand O atoms. C = black; H = white; N = blue; O = red; F = turquoise; Ni = purple.



**Crystallographic Studies:** A single crystal of  $p$ - $tbu$ dhbpy or Ni( $p$ - $tbu$ dhbpy) (**1**) was coated with Paratone oil and mounted on a MiTeGen MicroLoop. The X-ray intensity data for  $p$ - $tbu$ dhbpy were measured on a Bruker D8 Venture Kappa four-circle diffractometer system equipped with an Incoatec I $\mu$ S 3.0 micro-focus sealed X-ray tube (Cu K $\alpha$ ,  $\lambda = 1.54178$  Å) and a HELIOS MX double bounce multilayer mirror monochromator. The X-ray intensity data for Ni( $p$ - $tbu$ dhbpy) (**1**) were measured on a Bruker Kappa APEXII CCD system equipped with a fine-focus sealed tube (Mo K $\alpha$ ,  $\lambda = 0.71073$  Å) and a graphite monochromator. The frames were integrated with the Bruker SAINT software package<sup>23</sup> using a narrow-frame algorithm. Data were corrected for absorption effects using the Multi-Scan method (SADABS).<sup>23</sup> Each structure was solved and refined using the Bruker SHELXTL Software Package<sup>24</sup> within APEX3 or APEX4<sup>23</sup> and OLEX2.<sup>25</sup> Non-hydrogen atoms were refined anisotropically. The O-H hydrogen atoms were located in the diffraction map and refined with  $U_{iso} = 1.5U_{equiv}$  of the parent atom. All other hydrogen atoms were placed in geometrically calculated positions with  $U_{iso} = 1.2U_{equiv}$  of the parent atom ( $U_{iso} = 1.5U_{equiv}$  for methyl).

**Table S5:** Crystallographic details for  $p$ - $tbu$ dhbpy or Ni( $p$ - $tbu$ dhbpy) (**1**)

	$p$ - $tbu$ dhbpy	Ni( $p$ - $tbu$ dhbpy) ( <b>1</b> )
CCDC number	2155072	2155073
Formula	C <sub>30</sub> H <sub>32</sub> N <sub>2</sub> O <sub>2</sub>	C <sub>31</sub> H <sub>34</sub> N <sub>2</sub> NiO <sub>3</sub>
FW (g/mol)	452.57	541.31
Temp (K)	100(2)	100(2)
$\lambda$ (Å)	1.54178	0.71073
Size (mm)	0.052 x 0.230 x 0.400	0.026 x 0.066 x 0.736
Crystal habit	colorless plate	red needle
Crystal system	monoclinic	triclinic
Space group	P 2 <sub>1</sub> /c	P -1
a (Å)	17.9785(12)	7.1130(18)
b (Å)	6.9391(4)	11.635(3)
c (Å)	9.9776(6)	16.837(4)
$\alpha$ (°)	90	74.503(11)
$\beta$ (°)	105.218(4)	79.845(8)
$\gamma$ (°)	90	75.556(7)
Volume (Å <sup>3</sup> )	1201.10(13)	1291.3(6)
Z	2	2
Density (g/cm <sup>3</sup> )	1.251	1.392
$\mu$ (mm <sup>-1</sup> )	0.611	0.787
F(000)	484	572
$\theta$ range (°)	2.55 to 68.36	1.26 to 26.53
Index ranges	-21 $\leq$ h $\leq$ 21 -7 $\leq$ k $\leq$ 8 -12 $\leq$ l $\leq$ 12	-8 $\leq$ h $\leq$ 8 -14 $\leq$ k $\leq$ 14 -21 $\leq$ l $\leq$ 19
Reflns collected	21161	19569
Independent reflns	2202 [R <sub>int</sub> = 0.0568]	5300 [R <sub>int</sub> = 0.1076]
Data / restraints / parameters	2202 / 0 / 161	5300 / 0 / 344
GOF on F <sup>2</sup>	1.057	0.969
R <sub>1</sub> (I > 2 $\sigma$ (I))	0.0430	0.0553
wR <sub>2</sub> (all data)	0.0430	0.1374

## References

1. Hooe, S. L.; Dressel, J. M.; Dickie, D. A.; Machan, C. W. Highly Efficient Electrocatalytic Reduction of CO<sub>2</sub> to CO by a Molecular Chromium Complex. *ACS Catalysis* **2020**, 10 (2), 1146-1151 DOI: 10.1021/acscatal.9b04687.
2. Pegis, M. L.; Wise, C. F.; Martin, D. J.; Mayer, J. M. Oxygen Reduction by Homogeneous Molecular Catalysts and Electrocatalysts. *Chem. Rev.* **2018**, 118 (5), 2340-2391 DOI: 10.1021/acs.chemrev.7b00542.
3. Pegis, M. L.; Roberts, J. A. S.; Wasylenko, D. J.; Mader, E. A.; Appel, A. M.; Mayer, J. M. Standard Reduction Potentials for Oxygen and Carbon Dioxide Couples in Acetonitrile and N,N-Dimethylformamide. *Inorg. Chem.* **2015**, 54 (24), 11883-11888 DOI: 10.1021/acs.inorgchem.5b02136.
4. Kütt, A.; Tshepelevitsh, S.; Saame, J.; Lõkov, M.; Kaljurand, I.; Selberg, S.; Leito, I. Strengths of Acids in Acetonitrile. *European Journal of Organic Chemistry* **2021**, 2021 (9), 1407-1419 DOI: <https://doi.org/10.1002/ejoc.202001649>.
5. Frisch, M. J.; Trucks, G. W.; Schlegel, H. B.; Scuseria, G. E.; Robb, M. A.; Cheeseman, J. R.; Scalmani, G.; Barone, V.; Petersson, G. A.; Nakatsuji, H.; Li, X.; Caricato, M.; Marenich, A. V.; Bloino, J.; Janesko, B. G.; Gomperts, R.; Mennucci, B.; Hratchian, H. P.; Ortiz, J. V.; Izmaylov, A. F.; Sonnenberg, J. L.; Williams; Ding, F.; Lipparini, F.; Egidi, F.; Goings, J.; Peng, B.; Petrone, A.; Henderson, T.; Ranasinghe, D.; Zakrzewski, V. G.; Gao, J.; Rega, N.; Zheng, G.; Liang, W.; Hada, M.; Ehara, M.; Toyota, K.; Fukuda, R.; Hasegawa, J.; Ishida, M.; Nakajima, T.; Honda, Y.; Kitao, O.; Nakai, H.; Vreven, T.; Throssell, K.; Montgomery Jr., J. A.; Peralta, J. E.; Ogliaro, F.; Bearpark, M. J.; Heyd, J. J.; Brothers, E. N.; Kudin, K. N.; Staroverov, V. N.; Keith, T. A.; Kobayashi, R.; Normand, J.; Raghavachari, K.; Rendell, A. P.; Burant, J. C.; Iyengar, S. S.; Tomasi, J.; Cossi, M.; Millam, J. M.; Klene, M.; Adamo, C.; Cammi, R.; Ochterski, J. W.; Martin, R. L.; Morokuma, K.; Farkas, O.; Foresman, J. B.; Fox, D. J. *Gaussian 16 Rev. C.01*, Wallingford, CT, 2016.
6. Becke, A. D. Density-functional thermochemistry. III. The role of exact exchange. *J. Chem. Phys.* **1993**, 98 (7), 5648-5652 DOI: <http://dx.doi.org/10.1063/1.464913>.
7. Vosko, S. H.; Wilk, L.; Nusair, M. Accurate spin-dependent electron liquid correlation energies for local spin density calculations: a critical analysis. *Can. J. Phys.* **1980**, 58 (8), 1200-1211 DOI: 10.1139/p80-159.
8. Lee, C.; Yang, W.; Parr, R. G. Development of the Colle-Salvetti correlation-energy formula into a functional of the electron density. *Phys. Rev. B* **1988**, 37 (2), 785-789.
9. Stephens, P. J.; Devlin, F. J.; Chabalowski, C. F.; Frisch, M. J. Ab Initio Calculation of Vibrational Absorption and Circular Dichroism Spectra Using Density Functional Force Fields. *J. Phys. Chem.* **1994**, 98 (45), 11623-11627 DOI: 10.1021/j100096a001.
10. Hehre, W. J.; Lathan, W. A. Self-Consistent Molecular Orbital Methods. XIV. An Extended Gaussian-Type Basis for Molecular Orbital Studies of Organic Molecules. Inclusion of Second Row Elements. *The Journal of Chemical Physics* **1972**, 56 (11), 5255-5257 DOI: 10.1063/1.1677028.
11. Hariharan, P. C.; Pople, J. A. The influence of polarization functions on molecular orbital hydrogenation energies. *Theoretica chimica acta* **1973**, 28 (3), 213-222 DOI: 10.1007/BF00533485.
12. Francl, M. M.; Pietro, W. J.; Hehre, W. J.; Binkley, J. S.; Gordon, M. S.; DeFrees, D. J.; Pople, J. A. Self-consistent molecular orbital methods. XXIII. A polarization-type basis set for

- second-row elements. *The Journal of Chemical Physics* **1982**, 77 (7), 3654-3665 DOI: 10.1063/1.444267.
13. Grimme, S.; Antony, J.; Ehrlich, S.; Krieg, H. A consistent and accurate ab initio parametrization of density functional dispersion correction (DFT-D) for the 94 elements H-Pu. *J. Chem. Phys.* **2010**, 132 (15), 154104 DOI: doi:<http://dx.doi.org/10.1063/1.3382344>.
  14. Marenich, A. V.; Cramer, C. J.; Truhlar, D. G. Universal Solvation Model Based on Solute Electron Density and on a Continuum Model of the Solvent Defined by the Bulk Dielectric Constant and Atomic Surface Tensions. *The Journal of Physical Chemistry B* **2009**, 113 (18), 6378-6396 DOI: 10.1021/jp810292n.
  15. Ribeiro, R. F.; Marenich, A. V.; Cramer, C. J.; Truhlar, D. G. Use of Solution-Phase Vibrational Frequencies in Continuum Models for the Free Energy of Solvation. *The Journal of Physical Chemistry B* **2011**, 115 (49), 14556-14562 DOI: 10.1021/jp205508z.
  16. Funes-Ardoiz, I. P. R. S. *Goodvibes: Goodvibes 2.0.2*, v2.0.2; Zendo: 2016.
  17. DuBois, D. L. Development of Molecular Electrocatalysts for Energy Storage. *Inorganic Chemistry* **2014**, 53 (8), 3935-3960 DOI: 10.1021/ic4026969.
  18. Moreno, J. J.; Hooe, S. L.; Machan, C. W. DFT Study on the Electrocatalytic Reduction of CO<sub>2</sub> to CO by a Molecular Chromium Complex. *Inorganic Chemistry* **2021**, 60 (6), 3635-3650 DOI: 10.1021/acs.inorgchem.0c03136.
  19. Hooe, S. L.; Rheingold, A. L.; Machan, C. W. Electrocatalytic Reduction of Dioxygen to Hydrogen Peroxide by a Molecular Manganese Complex with a Bipyridine-Containing Schiff Base Ligand. *J. Am. Chem. Soc.* **2018**, 140 (9), 3232-3241 DOI: 10.1021/jacs.7b09027.
  20. Elgrishi, N.; Rountree, K. J.; McCarthy, B. D.; Rountree, E. S.; Eisenhart, T. T.; Dempsey, J. L. A Practical Beginner's Guide to Cyclic Voltammetry. *Journal of Chemical Education* **2018**, 95 (2), 197-206 DOI: 10.1021/acs.jchemed.7b00361.
  21. McKinnon, M.; Rochford, J. In *Green Chemistry*; Török, B., Dransfield, T., Ed.; Elsevier: 2018; pp 695-727.
  22. Sathrum, A. J.; Kubiak, C. P. Kinetics and Limiting Current Densities of Homogeneous and Heterogeneous Electrocatalysts. *The Journal of Physical Chemistry Letters* **2011**, 2 (18), 2372-2379 DOI: 10.1021/jz2008227.
  23. Saint, S. APEX3, Bruker AXS Inc. *Madison, WI, USA* **2012**.
  24. Sheldrick, G. SHELXT - Integrated space-group and crystal-structure determination. *Acta Cryst. A* **2015**, 71 (1), 3-8 DOI: doi:10.1107/S2053273314026370.
  25. Dolomanov, O. V.; Bourhis, L. J.; Gildea, R. J.; Howard, J. A. K.; Puschmann, H. OLEX2: a complete structure solution, refinement and analysis program. *J. Appl. Cryst.* **2009**, 42 (2), 339-341 DOI: doi:10.1107/S0021889808042726.